UC Irvine
UC Irvine Previously Published Works

Title

A cellular and molecular spatial atlas of dystrophic muscle.

Permalink

https://escholarship.org/uc/item/2dr068fv

Journal

Proceedings of the National Academy of Sciences, 120(29)

Authors

Stec, Michael

Su, Qi

Adler, Christina

et al.

Publication Date

2023-07-18

DOI

10.1073/pnas.2221249120

Peer reviewed

A cellular and molecular spatial atlas of dystrophic muscle

Michael J. Stec[a,1,2] (ID), Qi Su[a,1], Christina Adler[a], Lance Zhang[a], David R. Golann[a], Naveen P. Khan[a], Lampros Panagis[a], S. Armando Villalta[b,c,d] (ID), Min Ni[a], Yi Wei[a], Johnathon R. Walls[a], Andrew J. Murphy[a], George D. Yancopoulos[a], Gurinder S. Atwal[a], Sandra Kleiner[a], Gabor Halasz[a] (ID), and Mark W. Sleeman[a] (ID)

Asynchronous skeletal muscle degeneration/regeneration is a hallmark feature of Duchenne muscular dystrophy (DMD); however, traditional -omics technologies that lack spatial context make it difficult to study the biological mechanisms of how asynchronous regeneration contributes to disease progression. Here, using the severely dystrophic D2-mdx mouse model, we generated a high-resolution cellular and molecular spatial atlas of dystrophic muscle by integrating spatial transcriptomics and single-cell RNAseq datasets. Unbiased clustering revealed nonuniform distribution of unique cell populations throughout D2-mdx muscle that were associated with multiple regenerative timepoints, demonstrating that this model faithfully recapitulates the asynchronous regeneration observed in human DMD muscle. By probing spatiotemporal gene expression signatures, we found that propagation of inflammatory and fibrotic signals from locally damaged areas contributes to widespread pathology and that querying expression signatures within discrete microenvironments can identify targetable pathways for DMD therapy. Overall, this spatial atlas of dystrophic muscle provides a valuable resource for studying DMD disease biology and therapeutic target discovery.

Duchenne muscular dystrophy | spatial transcriptomics | asynchronous regeneration | skeletal muscle

Duchenne muscular dystrophy (DMD) is a severe muscle degenerative disease caused by mutations in the dystrophin gene, resulting in myofiber membrane instability and persistent muscle damage. Over time, chronic muscle damage in DMD patients leads to regenerative failure and replacement of muscle tissue with fibrotic and fatty infiltrates, ultimately leading to severe weakness, loss of ambulation, and cardiorespiratory failure. Recent advances in exon-skipping antisense oligonucleotide and gene therapy approaches to treat DMD have shown some evidence of de novo production of semifunctional dystrophin, although the efficacy and safety of these therapies remain to be significantly improved (1–4). Similarly, while the current standard of care treatment for DMD patients, systemic glucocorticoid administration, has demonstrated clear benefit in preserving muscle function and prolonging lifespan (5), the significant off-target effects of high-dose glucocorticoids prevent many DMD patients from initiating or continuing glucocorticoid treatment regimens (6).

While novel alternatives to conventional glucocorticoids may suppress muscle inflammation with some reduced side effects (e.g., vamorolone ref. 7), the identification of relevant pathways regulating disease biology could lead to the development of more targeted and effective anti-inflammatory therapies. Heightened muscle inflammation due to myofiber damage is a common feature of DMD, and a chronic proinflammatory environment contributes to exacerbated muscle damage (reviewed in ref. 8). Unlike an acute muscle injury in which there is a highly coordinated regenerative response of immune, fibrogenic, and myogenic cells (9), muscle injury in DMD is constant and asynchronous, leading to chronic inflammation and fibrosis. Seminal work from the Hoffman laboratory (10) using laser capture microdissection demonstrated that multiple asynchronous muscle injuries within localized microenvironments lead to diffuse inflammatory and fibrotic signaling, thus implicating asynchronous degeneration as a likely contributor to muscle pathology in DMD.

Given that muscle damage is nonuniformly distributed throughout DMD muscle and that damage, inflammation, and regeneration are asynchronous in nature in the context of DMD, it is difficult to study spatiotemporal mechanisms that drive disease progression. While bulk and single-nucleus transcriptomics profiling have been used to identify pathways that are broadly altered in dystrophic muscle (11–16), these techniques lack spatial resolution and are unable to provide a clear picture of the cell types and molecular signaling events within discrete microenvironments of dystrophic tissue. Spatial transcriptomics profiling, which maps gene expression signatures to histological sections, is well suited for studying cellular and molecular mechanisms driving dystrophic disease progression, as it

Significance

Duchenne muscular dystrophy (DMD) is a severe genetic muscle disease in which loss of the dystrophin protein results in myofiber membrane instability and persistent, asynchronous muscle damage. Due to the asynchronous nature of DMD, it is difficult to study spatiotemporal mechanisms that drive disease progression using conventional -omics technologies. Here, we coupled spatial transcriptomics with single-cell RNAseq and found that specific proinflammatory signals and fibrotic cells are associated with discrete tissue areas at different stages of regeneration and that these signals/cells spread throughout the surrounding tissue. These findings provide insight on biological mechanisms mediating chronic inflammatory conditions such as DMD and offer a tool for identification of targetable pathways for therapeutic development for these diseases.

allows for visualization of gene expression within the native muscle tissue environment. This technology has recently been utilized to generate valuable resources for exploring spatial gene expression and cellular processes in injured and denervated skeletal muscle (17, 18), and the findings from these studies suggest that it may provide a unique platform for studying dystrophic disease biology.

Here, we leveraged spatial and single-cell transcriptomics technologies to generate a high-resolution molecular atlas of dystrophic mouse muscle tissue. We found that the severely dystrophic D2-mdx mouse model closely mimics the asynchronous degeneration/regeneration pathology seen in human DMD muscle and we were able to clearly define spatiotemporal gene expression patterns and cell types associated with different stages of regeneration in this model. Using this spatial dataset, we found that proinflammatory signals from recently damaged areas and profibrotic cells from actively regenerating areas were propagated throughout the surrounding tissue. Overall, this cellular and molecular spatial atlas of dystrophic muscle provides a powerful tool for studying disease biology and identifying potential therapeutic targets for the treatment of DMD.

Results

Spatial Transcriptomics Profiling Reveals Distinct Cell-Type Organization in Homeostatic Mouse Skeletal Muscle. To explore spatial gene expression patterns within homeostatic and chronically damaged muscle tissue, we performed global spatial transcriptomics profiling on cryosections of the gastrocnemius/plantaris complex of 6-wk-old wild-type (DBA2/J; WT) and severely dystrophic (D2-mdx; referred to as MDX) mice (Fig. 1A). In brief, muscle was cryosectioned onto Visium spatial gene expression slides, fixed, H&E stained and imaged, and subsequently permeabilized to allow release and binding of mRNA to spatially barcoded capture probes. cDNA synthesized from captured mRNA was then sequenced and expression data were mapped back to imaged sections. Adjacent serial tissue sections from each sample were collected for follow-up immunostaining and in situ hybridization (ISH) analysis. On average, we detected 1476 mRNA-capture probe spots (55 μm diameter each) per WT sample (n = 3) that were covered by tissue. A median depth of 287,498 reads were sequenced per spot of the WT samples, containing a median of 2,779 detected genes, with an overall median of 16,692 genes detected per sample (Dataset S1). Expression matrices were combined from all WT samples; then, gene and spot filtering, dimensionality reduction, and clustering of all spots were performed. We identified 11 clusters that were spatially mapped to H&E-stained samples (Fig. 1B and SI Appendix, Fig. S1).

Cell types defining each cluster were inferred based on expression of canonical genes (Fig. 1C and Dataset S2). As expected, myofibers comprised the most spots in WT muscle and were categorized as Type IIb, Type IIx, Type IIa, and Type I based on their expression of contractile and metabolic genes. For example, fast-twitch muscle genes (e.g., *Myh4, Myl1,* and *Pvalb*) were most highly expressed in Type IIb clusters, whereas slow-twitch muscle genes (e.g., *Myh7, Myl2,* and *Tnnt1*) were most highly expressed in Type I clusters. The expression of metabolic enzymes followed a similar pattern, with muscle creatine kinase (*Ckm*) most highly expressed in Type IIb clusters and myoglobin (*Mb*) most highly expressed in Type I clusters. The gradient expression pattern of contractile, metabolic, and mitochondrial genes across the myofiber clusters was consistent with the well-described fiber-type continuum (i.e., fast-twitch glycolytic→slow-twitch oxidative: IIb→IIx→IIa→I).

In addition to these myofiber types, we also identified clusters that were enriched for gene expression signatures of other cell populations, although all clusters identified contained some degree of myofiber gene signature due to the mRNA-capture probe size. We noted subsets of myofibers that appeared to have an enriched red blood cell (RBC) gene signature (fast fiber + RBC and slow fiber + RBC clusters), indicated by high expression of hemoglobin and erythroid genes (e.g., *Hba-a1, Hbb-bs,* and *Alas2*), along with their respective fiber-type markers. Interestingly, D'Ercole et al. (18) noted areas of mouse tibialis anterior muscle with a strikingly similar gene expression profile that they hypothesized could be attributed to these areas containing small blood vessels. To further explore whether Slow/Fast fiber + RBC cluster areas were indeed enriched for blood vessels/capillaries, we performed immunofluorescence-coupled spatial transcriptomics using a CD31 antibody. Surprisingly, when examining areas with high expression of *Alas2* (the top significantly expressed erythroid marker of this cluster), we did not find that these areas were enriched for CD31$^+$ blood vessels/capillaries compared to the rest of the tissue (SI Appendix, Fig. S2). Thus, these clusters are not unique in their total abundance of blood vessels or capillaries; rather, they may potentially represent areas of tissue with altered microvascular perfusion dynamics, leading to accumulation of RBCs at the time of tissue collection.

We identified several other clusters with clear gene signatures, including fibroblast/tenocyte clusters (Fibro./Teno.) expressing high levels of extracellular matrix proteins (e.g., *Col1a1, Col1a2,* and *Fmod*), mesenchymal stromal progenitor cell clusters (MPC) that expressed smooth muscle and fibrogenic markers (e.g., *Acta2, Tagln, Myl9, Col3a1,* and *Gsn*), neuronal cell clusters (Nerve) that expressed myelinating genes (e.g., *Mpz, Pmp22,* and *Mbp*), neuromuscular junction clusters (NMJ) that expressed postsynaptic NMJ markers (e.g., *Chrna1* and *Chrne*), and clusters containing adipose genes (e.g., *Fasn* and *Scd1*) along with sporadic expression of blood vessel markers (e.g., *Hba-a1* and *Hba-bs*) which we termed blood vessel + perivascular adipose tissue clusters (BV + PVAT).

To further confirm the identity of these clusters, we aligned spatially mapped gene expression data with images of immunostained serial sections of corresponding samples. We found that the localization of myofiber-type clusters (Fig. 1D) corresponded with the myosin heavy chain gene (Fig. 1E) and protein (Fig. 1F) expression that defined each myofiber type. Other less abundant clusters also highly overlapped key histological features supporting cluster identity. For example, nerve and NMJ clusters (Fig. 1G) displayed discrete localization of genes defining each cluster (e.g., *Mpz* and *Chrna1*, respectively) (Fig. 1H), with nerve clusters spatially overlapping with large tibial and sural nerve bundles stained with neurofilament and NMJ clusters overlapping tissue areas containing groups of α-bungarotoxin$^+$ NMJs (Fig. 1I). Similarly, BV + PVAT clusters (Fig. 1J) displayed localized *Fasn* gene expression (Fig. 1K), and this cluster histologically aligned to the area of the saphenous vein at the superficial aspect of the gastrocnemius muscle and contained CD31$^+$ blood vessel structures surrounded by perilipin$^+$ adipose tissue (Fig. 1K). Finally, Fibro./Teno. cluster regions (Fig. 1J) were spatially mapped to areas surrounding and separating the gastrocnemius/plantaris muscles and displayed high levels of *Col1a1* expression and binding of wheat germ agglutinin (Fig. 1L), indicating a dense extracellular matrix network consistent with muscle epimysium. Altogether, these data show clear segregation of cell clusters based on unbiased gene expression profiling, with cluster identities confirmed by spatial localization and histological features, thereby validating spatial transcriptomics as a robust tool for profiling skeletal muscle tissue sections.
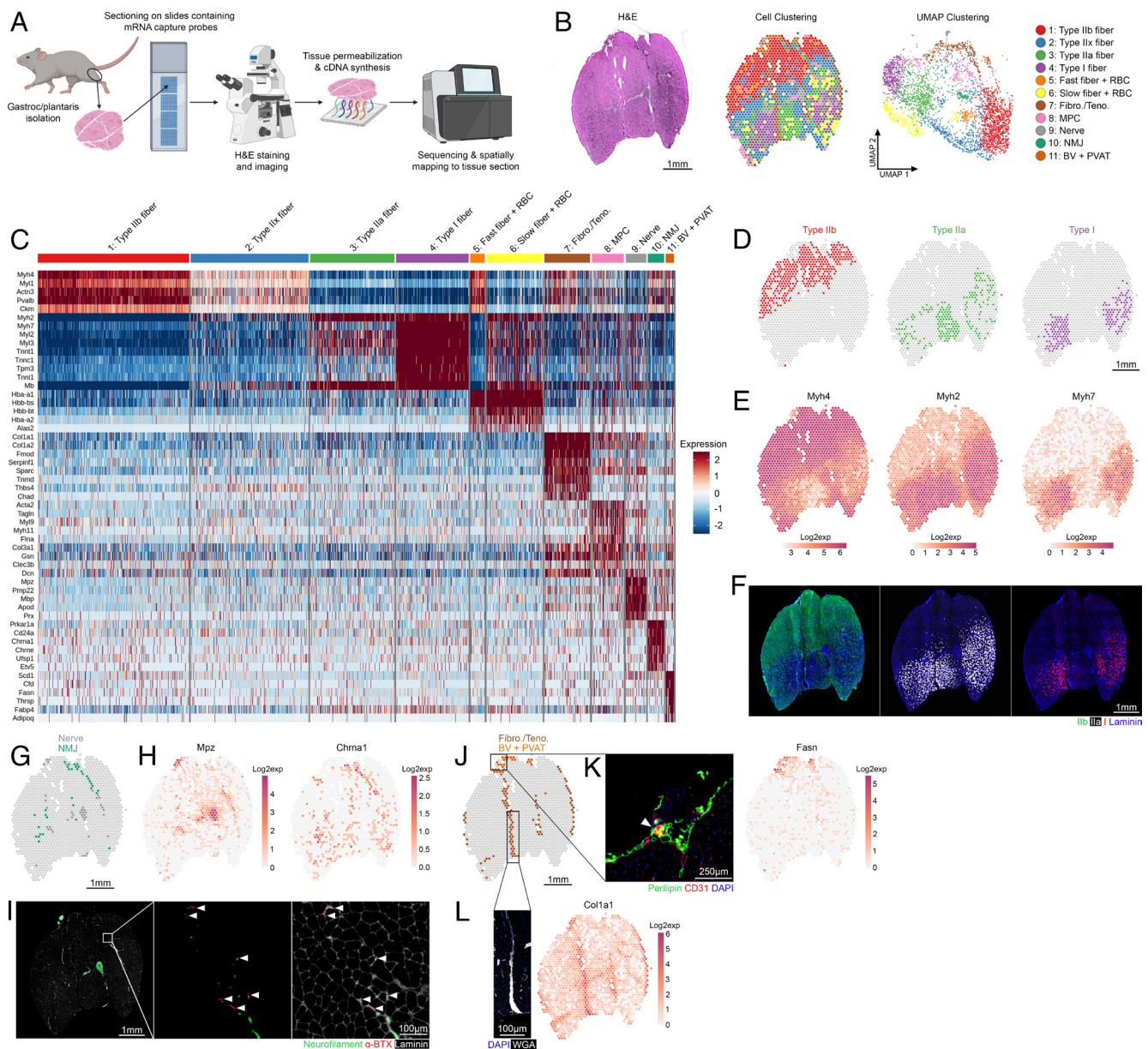
Fig. 1. Spatial transcriptomics profiling of skeletal muscle identifies multiple cell clusters within distinct locations. (A) Workflow of spatial gene expression profiling of mouse gastrocnemius/plantaris muscles. (B) H&E-stained WT hindlimb muscle from one representative sample (*Left*) with Visium spot transcriptome clusters visualized on tissue-covered area (*Center*) and as a UMAP plot (*Right*). The 11 unique clusters were identified from n = 3 WT muscle sections. (C) Heatmap showing top canonical markers defining each cell cluster. (D) Myofiber cluster identity displays high overlap with (E) spatial patterning of corresponding myosin heavy chain gene expression and (F) myosin heavy chain isoform protein localization in serial sections. (G) Nerve and NMJ clusters express high levels of (H) myelinating genes (e.g., *Mpz*) and postsynaptic NMJ genes (e.g., *Chrna1*), respectively. (I) Serial section immunostaining depicting enrichment for neurofilament-stained nerve bundles and α-bungarotoxin-stained NMJs. Arrows indicate NMJs within NMJ cluster areas as defined by spatial transcriptomics. (J) Fibro./Teno. clusters are enriched at the epimysium surrounding and separating the gastrocnemius/plantaris, and BV + PVAT clusters are enriched at the superficial gastrocnemius region associated with the saphenous vein. (K) Immunostaining of serial sections depicting large CD31+ blood vessels (arrow) at the muscle periphery with surrounding adipose tissue identified by perilipin staining and enrichment for adipocyte gene expression (e.g., *Fasn*) in BV + PVAT cluster areas. (L) Fibro./Teno. cluster regions show enrichment for ECM proteins, as assessed by wheat germ agglutinin staining of serial sections and by high expression of ECM genes (e.g., *Col1a1*).

Asynchronous Degeneration/Regeneration Is a Key Feature of D2-mdx Dystrophic Muscle. Persistent and nonuniform muscle degeneration is a hallmark of human dystrophic muscle; however, traditional -omics technologies (e.g., bulk and single-cell/nucleus RNAseq) are unable to fully capture the complex interplay between immune, fibrogenic, and myogenic cell types within the native dystrophic tissue environment. To spatially resolve cell populations involved in dystrophic disease progression, we performed spatial transcriptomics analysis on the gastrocnemius/plantaris complex of 6-wk-old MDX mice (n = 5). Similar to WT muscle, the optimal enzyme permeabilization time for maximal mRNA release

throughout MDX muscle was found to be 12 min, although tissue areas with dense fibrosis appeared to have less RNA release, potentially due to suboptimal permeabilization. However, spatial gene detection using serial sections that were permeabilized for different amounts of time found that increasing permeabilization time was not sufficient to release more RNA from highly fibrotic areas (*SI Appendix,* Fig. S3), suggesting that reduced transcript detection may not have been due to suboptimal permeabilization, but instead may be driven by reduced cell number in these regions.

In MDX samples, an average of 1,028 spots were covered by tissue, with a median read depth of 443,556 reads and 3,507 genes

detected per spot, with an overall median of 17,476 genes detected per sample (Dataset S1). MDX spots typically contained more genes and transcripts detected compared to WT, potentially due to higher cell diversity and density within damaged areas, as well as increased diversity of gene expression within myofibers. Indeed, unbiased clustering of MDX spatial data identified several immune and regenerative clusters not present in WT samples. Compared to the clear distribution patterns seen for myofibers, these MDX-specific clusters showed marked heterogeneity of cluster localization (Fig. 2A) and abundance (Fig. 2B) between MDX samples. Canonical gene expression signatures were used to annotate these four new cell clusters in MDX tissue: an immune cluster (Immune 1) expressing high levels of chemokine ligands (e.g., *Ccl2* and *Ccl7*), an immune cluster (Immune 2) expressing antigen-presenting cell (APC) genes (e.g., *Lyz2* and *Ctsk*), a regenerating myofiber cluster (Regn. fiber) expressing myogenic (e.g., *Myog*), fusogenic (e.g., *Mymk*), and developmental myosin (e.g., *Myh8* and *Myh3*) genes, and a cluster expressing both myofiber and Immune 1 genes, which we termed Fiber + inflamm. cluster (Fig. 2C and Dataset S2).

To further define immune cluster areas, we performed differential gene expression analysis on Immune 1 and Immune 2 cluster spots from all MDX samples. We found that Immune 1 clusters were enriched for pathways regulating granulocyte/neutrophil chemotaxis and migration, whereas Immune 2 clusters displayed signatures of APCs and extracellular structure organization (Fig. 2D). In addition to the dominant immune genes expressed in these clusters, we were able to identify significantly higher expression of myofiber contractile protein genes (e.g., *Des* and *Ttn*) in Immune 1 clusters and higher expression of extracellular matrix genes (e.g., *Col1a1*, *Col6a2*, and *Col3a1*) in Immune 2 clusters, potentially indicating characteristics of the microenvironment in which these immune cells reside (Fig. 2E).

To shed further light on the identity and tissue microenvironment of dystrophic cell clusters, we examined immunostained serial sections from regions corresponding to the clusters we defined (Fig. 2F). Consistent with spatial gene profiling, Immune 1 tissue areas consisted of dense cell populations invading recently damaged myofibers, indicated by intracellular mIgG staining (a marker of disrupted sarcolemma/necrotic fibers). Also, in accordance with their gene expression profile, Immune 2 tissue areas were devoid of myofibers and contained more F4/80$^+$ macrophages than Immune 1 areas. Finally, imaging of Regn. fiber clusters revealed small, newly formed myofibers surrounded by F4/80$^+$ macrophages. To gain a better understanding of the macrophage subtypes present within clusters, we performed immunostaining with pro- (CD68) and anti- (CD206) inflammatory macrophage markers. Surprisingly, CD206$^+$ anti-inflammatory macrophages were detected throughout the muscle interstitium but not present in Immune 1/2 areas (Fig. 2G). On the other hand, CD68+ proinflammatory macrophages were present in Immune 1 areas and were highly abundant in Immune 2 areas (Fig. 2G).

The strong concordance between unbiased spatial gene expression profiling and histological characterization allowed us to predict the regenerative state of each cluster (Fig. 2H). Immune 1 areas could be clearly defined as the earliest state of regeneration, with granulocyte infiltration and early signs of proinflammatory macrophage accumulation in regions of recently damaged myofibers. Immune 2 areas represented an intermediate stage of regeneration, where necrotic myofibers have been fully cleared by phagocytotic cells and proinflammatory macrophages are a dominant cell population. Finally, Regn. fiber areas depict a late stage of regeneration, evidenced by formation of nascent myofibers along with decreased immune cell infiltration. To further support

the regenerative states of these MDX clusters, we integrated gene module scores of Immune 1, Immune 2, and Regn. fiber clusters with spatial transcriptomics data that we obtained from injuring C57BL/6 mice with cardiotoxin and collecting muscle at 1, 3, and 5 d post injury (dpi) (Fig. 3A and Dataset S1). Interestingly, injured areas from 1 dpi shared gene expression features primarily with Immune 1 clusters, 3 dpi injured areas with Immune 2 clusters, and 5 dpi injured areas with Regn. fiber clusters, further supporting the regenerative states of these MDX clusters (Fig. 3B).

The regenerative phases evidenced by these cell clusters are partially in line with the well-described, synchronous process of skeletal muscle regeneration following injury (reviewed in ref. 19). However, during normal muscle regeneration, early infiltration of granulocytes (GN) and proinflammatory macrophages is followed by an increase in anti-inflammatory macrophage abundance to support myogenesis, which we did not observe in dystrophic tissue. Additionally, we noted a clear spatiotemporal defect in regeneration in these dystrophic muscles, where multiple cell clusters in different phases of regeneration appear distributed at random throughout the tissue. Thus, these findings support that a proinflammatory, asynchronously regenerating environment contributes to dystrophic muscle pathology in the D2-mdx mouse model.

Deconvolution of Spatial Transcriptomics Data Generates a High-Resolution Map of Cell Populations in Dystrophic Muscle.
The 55 μm spots used in our Visium platform are expected to contain multiple cells. To more precisely characterize the cellular landscape of the dystrophic muscle microenvironment, we computationally inferred the cell-type composition of each barcoded capture spot, leveraging a publicly available single-cell RNAseq dataset taken from uninjured and notexin-injured (2, 5, and 7 d postinjury, dpi) mouse muscle tissue (20). We first clustered and annotated this dataset, revealing 30 cell populations present in homeostatic and injured muscle, including: B cells (B), endothelial cells (Endo), fibroadipogenic progenitors (FAPs), myofibers (Fibers), fusing myoblasts (FuMb), granulocytes (GN), immunomyoblasts (ImMb), macrophages (Mac), muscle stem cells (MuSC), NK/T cells (NK/T), pericytes (Pericyte), Schwann cells (Schwann), smooth muscle cells (SMC), and tenocytes (Teno) (Fig. 4A, *SI Appendix,* Fig. S4, and Dataset S3). We then used this reannotated dataset to estimate cell-type proportion within each barcoded capture spot in WT and MDX spatial transcriptomes data via a stereoscope (21). Cell-type proximity maps were visualized as chord diagrams, revealing colocalization of multiple cell types within each spot in MDX muscle (Fig. 4B).

To explore the cellular microenvironment of damaged areas, we plotted cell-type prediction proportions for the most highly abundant cell types (excluding myofibers) in Immune 1, Immune 2, and Regn. fiber areas (Fig. 4C), along with spatial mapping of these cell types onto MDX tissue areas (Fig. 4 D–F). These data supported the regenerative state of each cluster inferred from our unbiased spatial profiling, while providing enhanced cellular resolution. For example, it is known that during the earliest state of muscle regeneration, GN (e.g., neutrophils and eosinophils) and proinflammatory macrophages are among the first cell types to invade damaged muscle, with the latter secreting cytokines and growth factors to promote MuSC proliferation (19, 22–24). In Immune 1 areas, which represent the earliest state of regeneration, cellular deconvolution estimated a high proportion of GN and proliferating MuSCs (MuSC2; expressing *Myod1*, *Myog*, and *Mki67*), as would be expected at this early stage of regeneration (Fig. 4D). In Immune 2 areas, we predicted an increase of Mac2 and Mac4, which are macrophage populations most abundant at 5 d post injury in wild-type mice (*SI Appendix,* Fig. S4),
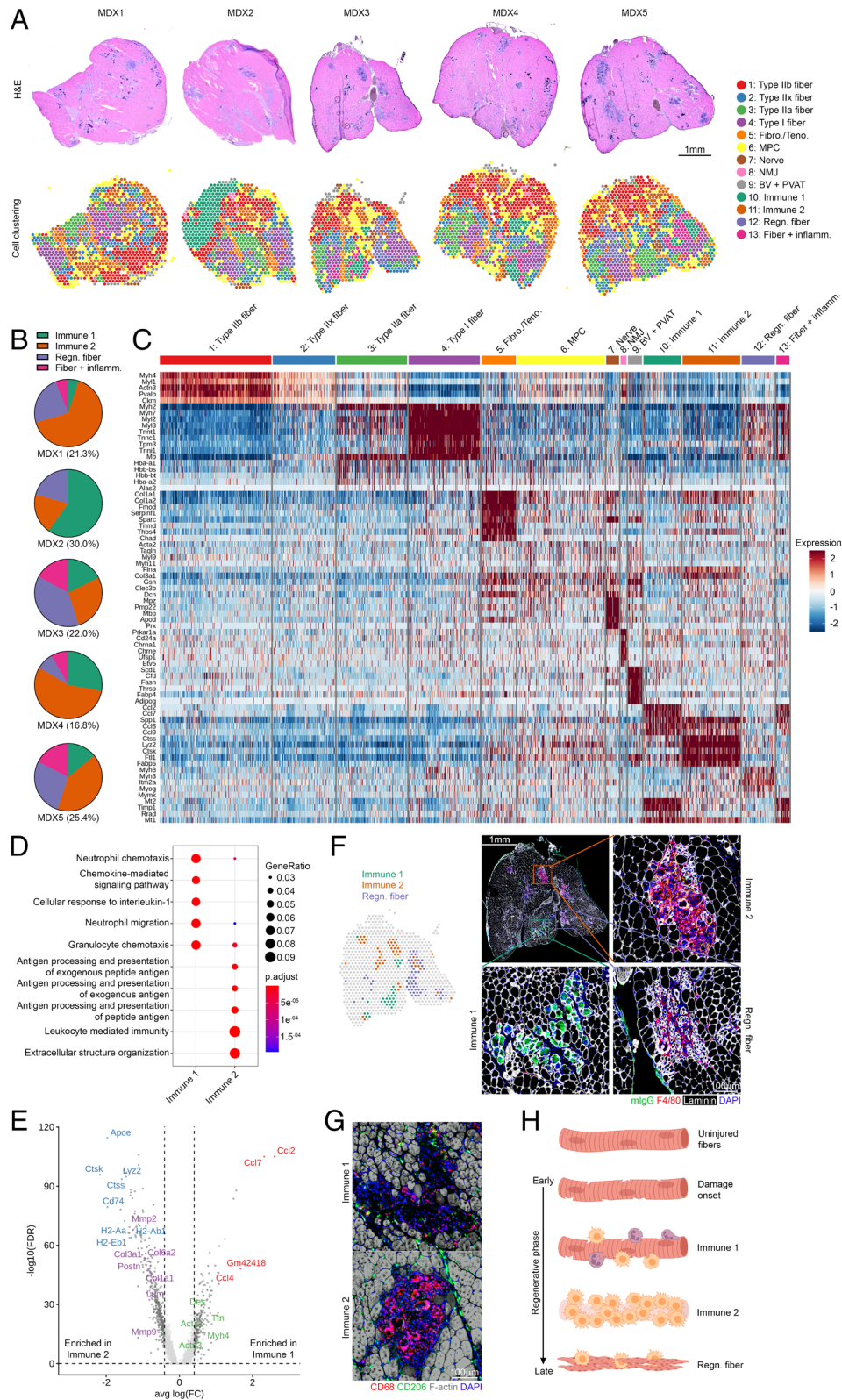
Fig. 2. Mapping asynchronous regeneration of dystrophic muscle by spatial gene profiling. (*A*) Unbiased clustering of gene expression profiling identified 13 unique clusters in MDX hindlimb muscle (n = 5) that were mapped to H&E-stained tissue sections. (*B*) Distribution of immune and regenerative clusters among each MDX sample, with the total spot proportion of these four clusters denoted in parentheses. (*C*) Heatmap showing top canonical markers defining each cell cluster. (*D*) Top five Gene Ontology pathways (biological process) enriched in Immune 1 and Immune 2 clusters. Gene ratio is the total number of DEGs divided by the total number of genes in each geneset, and the adjusted *P* value is based on gene set enrichment analysis. (*E*) Volcano plot highlighting differential expression of immune (red, blue), myofilament (green), and ECM genes (purple) between Immune 1 and Immune 2 clusters. (*F*) Cell cluster localization of Immune 1, Immune 2, and Regn. fiber clusters with serial immunostaining for markers of damaged myofibers (mIgG) and macrophages (F4/80). (*G*) Immunostaining for pro- (CD68) and anti- (CD206) inflammatory macrophages in Immune 1 and Immune 2 cluster areas. (*H*) Schematic depicting the state of regeneration of spatially defined MDX clusters, with granulocytes depicted in purple and macrophages depicted in orange.
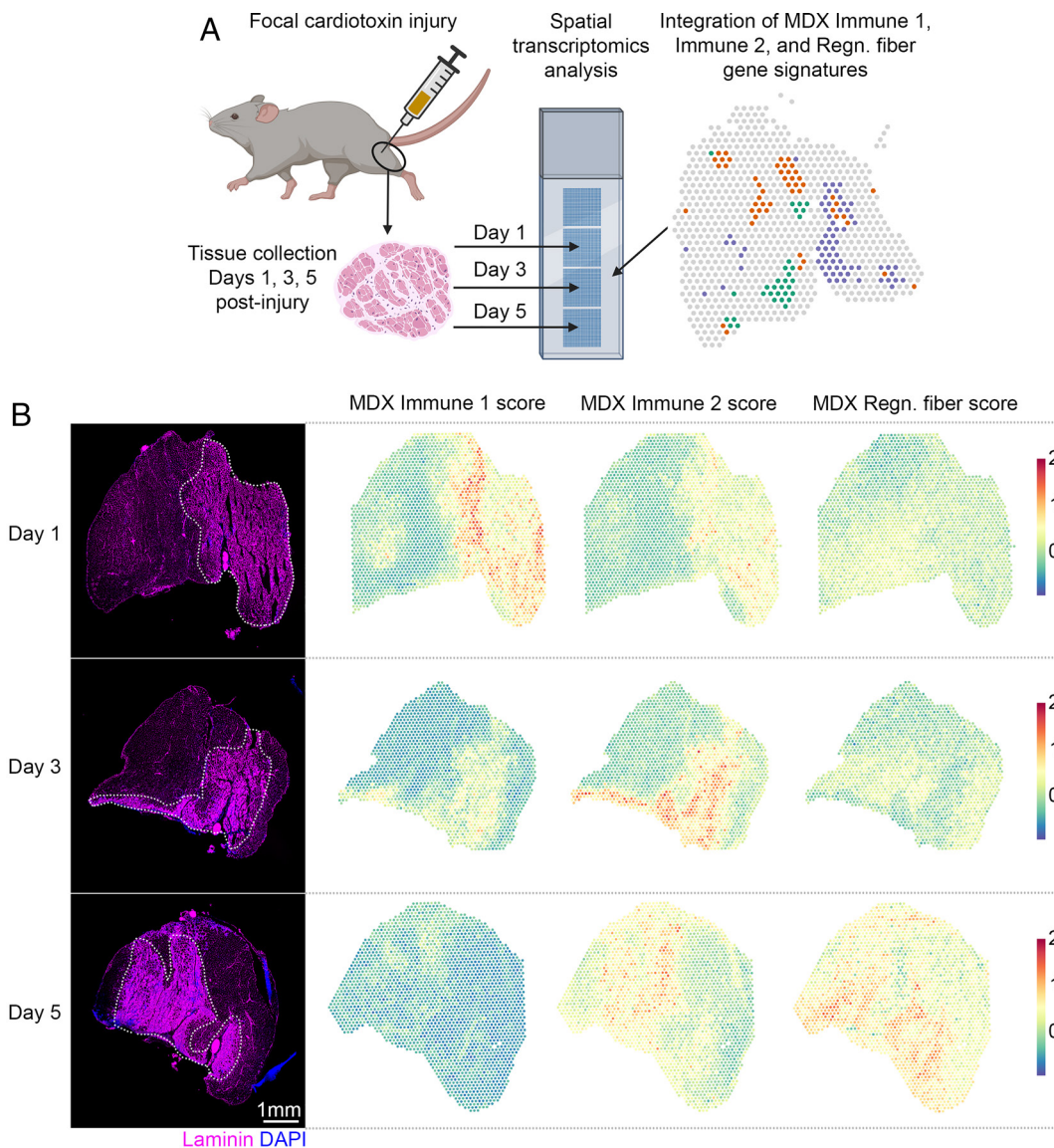
Fig. 3. Gene expression signatures from unique dystrophic muscle areas align with distinct timepoints of regeneration. (*A*) Schematic depicting focal cardiotoxin injury of WT mice and integration of MDX cluster gene signatures with spatial transcriptomics datasets obtained at multiple timepoints following injury. (*B*) Immunostaining images depicting focal areas of cardiotoxin-induced damage (dotted lines) at different timepoints and expression scores of MDX Immune 1, Immune 2, and Regn. fiber clusters plotted on injured tissue at each timepoint.

supporting that Immune 2 areas are in an intermediate stage of regeneration (Fig. 4*E*). Finally, fusing myoblasts (FuMb) and pericytes, both of which regulate nascent myofiber formation, were predicted to be most abundant in Regn. fiber areas, confirming that these areas are in a late stage of regeneration (Fig. 4*F*). Cell-type deconvolution and spatial mapping of the entire tissue area was performed with all 30 single-cell populations, thus providing a high-resolution cellular atlas of dystrophic muscle (*SI Appendix*, Fig. S5). Overall, by integrating single-cell RNAseq data with spatial transcriptomics profiling, we have generated a comprehensive spatial database of the dystrophic tissue microenvironment that can be queried to explore how local cell–cell communication contributes to dystrophic disease progression.

Spatial Profiling Identifies Signals Driving Inflammation and Fibrosis in Dystrophic Muscle. In DMD, focal myofiber necrosis in discrete areas ultimately leads to widespread pathological changes (e.g., myofiber atrophy, inflammation, and fibrosis) throughout the entire muscle tissue. The Hoffman laboratory

(10) provided evidence that asynchronous regeneration from multiple focal muscle injuries leads to heightened inflammatory and fibrotic signaling in uninjured muscle between damaged areas in healthy mice. Thus, the propagation of signals from locally damaged areas throughout the surrounding undamaged tissue is likely a central driver of widespread inflammation and fibrosis in dystrophic muscle. To explore pathways regulating pathological changes in regions without overt muscle damage, we performed differential gene expression analysis on the Type IIb myofiber spots between WT and MDX samples (Fig. 5*A* and Dataset S4). Among the 220 up-regulated and 25 down-regulated genes in the MDX Type IIb myofiber spots, pathway analysis revealed strong enrichment for fibrotic and immune pathways within these regions (Fig. 5*B*), indicating that signals from damaged/regenerating areas are potentially spread to distant undamaged areas of dystrophic muscle. Similar changes in gene expression and pathway regulation were observed in other myofiber-type clusters, indicating broad inflammatory/fibrotic signals throughout the muscle (*SI Appendix*, Fig. S6 and Dataset S4).
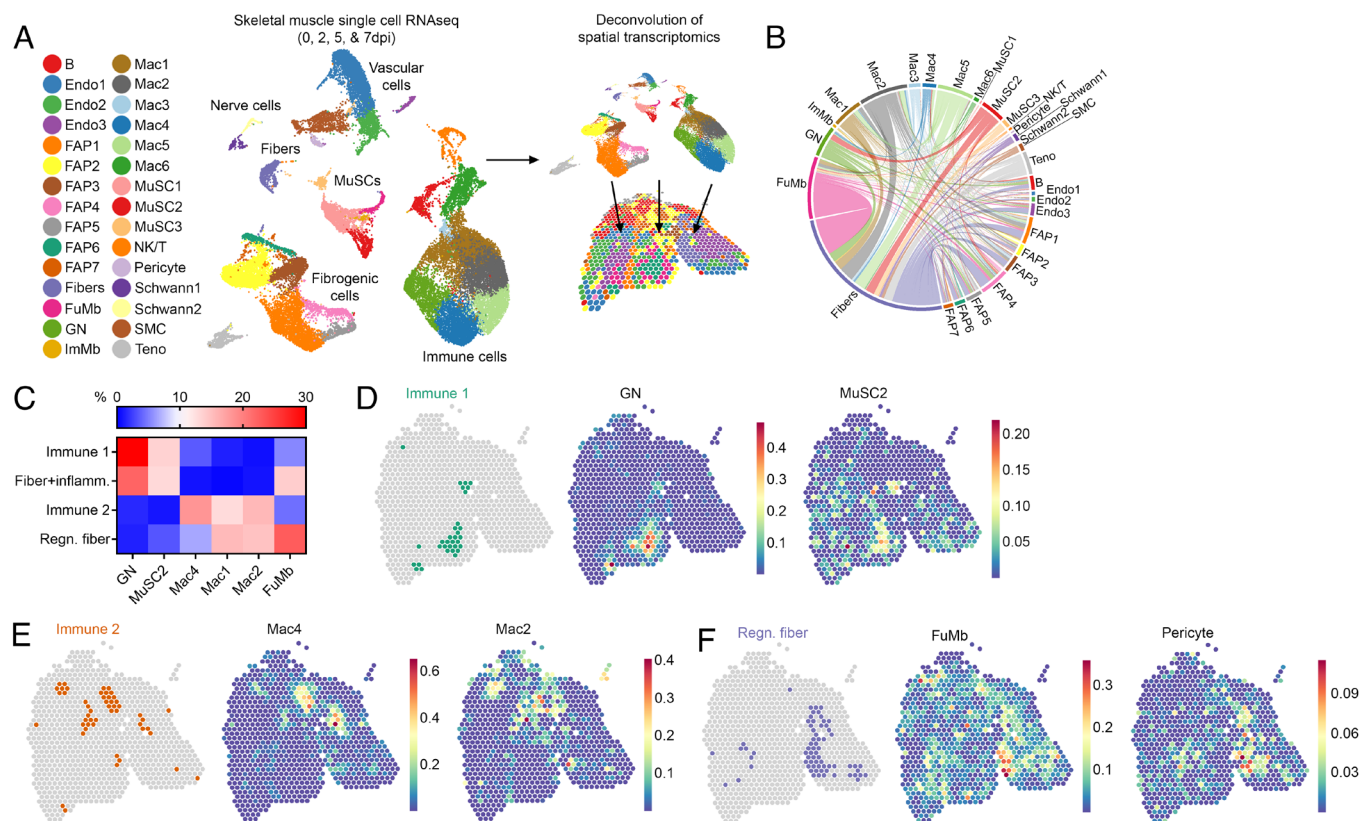
Fig. 4. Single-cell deconvolution of spatial transcriptomics data in dystrophic muscle. (*A*) Reclustering of skeletal muscle single-cell RNAseq from De Micheli et al. (20) and integration with spatial transcriptomics of dystrophic muscle. (*B*) Chord diagram displaying co-occurrence of inferred cell types in dystrophic muscle. (*C*) Heatmap showing the proportion of inferred cell types present within spatial clusters (excluding myofibers). Representative spatial localization and abundance of inferred cell types within Immune 1 (*D*), Immune 2 (*E*), and Regn. fiber (*F*) areas of dystrophic muscle.

To further explore how local muscle damage may signal to surrounding tissue to promote widespread pathology, we investigated spatial patterns of cell clusters associated with damaged areas by calculating neighborhood enrichment scores based on proximity on the connectivity graph of spot clusters (via Spatial Quantification of Molecular Data in Python; Squidpy) (25). Neighborhood enrichment analysis (Fig. 5*C*) of spatial transcriptomics clusters revealed enrichment (i.e., positive z-scores) for cluster pairs: Type IIx—Type IIa, Immune 2—MPC, and Immune 1—Fiber + inflamm. (Fig. 5 *D* and *E* and *SI Appendix,* Fig. S7), indicating that these cluster pairs were within close spatial proximity of each other. Enrichment of Type IIx and Type IIa neighborhoods validated this analysis, as these two myofiber types are found in close proximity of each other in the plantaris and deep gastrocnemius muscles (Fig. 5*A*). To follow up on the predicted spatial enrichment of Immune 2—MPC and Immune 1—Fiber + inflamm. cluster pairs, we manually quantified the proportion of peripheral immune cluster spots that were adjacent to their respective predicted cluster pair. Interestingly, we found that the majority of Immune 2 cluster spots on the edge of damaged regions were directly adjacent to MPC clusters (Fig. 5*F*). Consistent with the expression of ECM genes observed in Immune 2 (Fig. 2*C*), we observed a significant amount of fibrosis within Immune 2 area spots relative to the rest of the tissue (Fig. 5 *G* and *H*), suggesting that fibrogenic cells/signals within Immune 2 areas may be a source for the heightened amount of MPC clusters adjacent to these regions. The abundance of skeletal muscle MPCs (e.g., fibroadipogenic progenitors, FAPs) is temporally regulated during muscle regeneration, and persistent FAP accumulation correlates with fibrotic severity in DMD muscle (16, 26, 27). Aside from

their unique spatial localization adjacent to Immune 2 cluster areas, we found that there were significantly more total MPC cluster spots present within MDX tissue compared to WT (Fig. 5*I*). Pdgfra (a marker of FAPs) immunostaining revealed that FAP accumulation is first observed in areas of early regeneration (Immune 1), followed by massive accumulation in intermediate stages of regeneration (Immune 2), with subsequent clearance of the FAP population in late-stage regeneration (Regn. fiber) (*SI Appendix,* Fig. S8), consistent with the described temporal appearance and clearance of FAPs in injured muscle (28, 29). Importantly, Pdgfra+ FAPs were present in MPC spot areas directly surrounding Immune 2 spots (Fig. 5*J*) confirming the cellular identity of the MPC spot population and demonstrating that FAPs can spread from damaged areas into undamaged areas in MDX tissue. Overall, these data show that macrophage-rich Immune 2 areas contain an abundance of FAPs and dense fibrosis and that propagation of FAPs away from these regenerating areas into undamaged tissue likely contributes to widespread fibrosis in dystrophic muscle.

Next, we sought to determine whether more recently damaged areas (Immune 1 clusters) also signal to nearby tissue (Fiber + inflamm. clusters) to exacerbate dystrophic muscle pathology. Supporting our Squidpy neighborhood enrichment analysis, manual quantification of peripheral Immune 1 spots revealed that these spots were frequently surrounded by Fiber + inflamm. cluster spots (Fig. 5*K*), which displayed a gene expression profile of Immune 1 cluster spots along with myofiber gene signatures (Fig. 2*C*), indicating spillover of immune cells/signals into surrounding undamaged tissue. The top three genes expressed in Immune 1 clusters were *Ccl2*, *Ccl7*, and *Spp1*, and their expression was
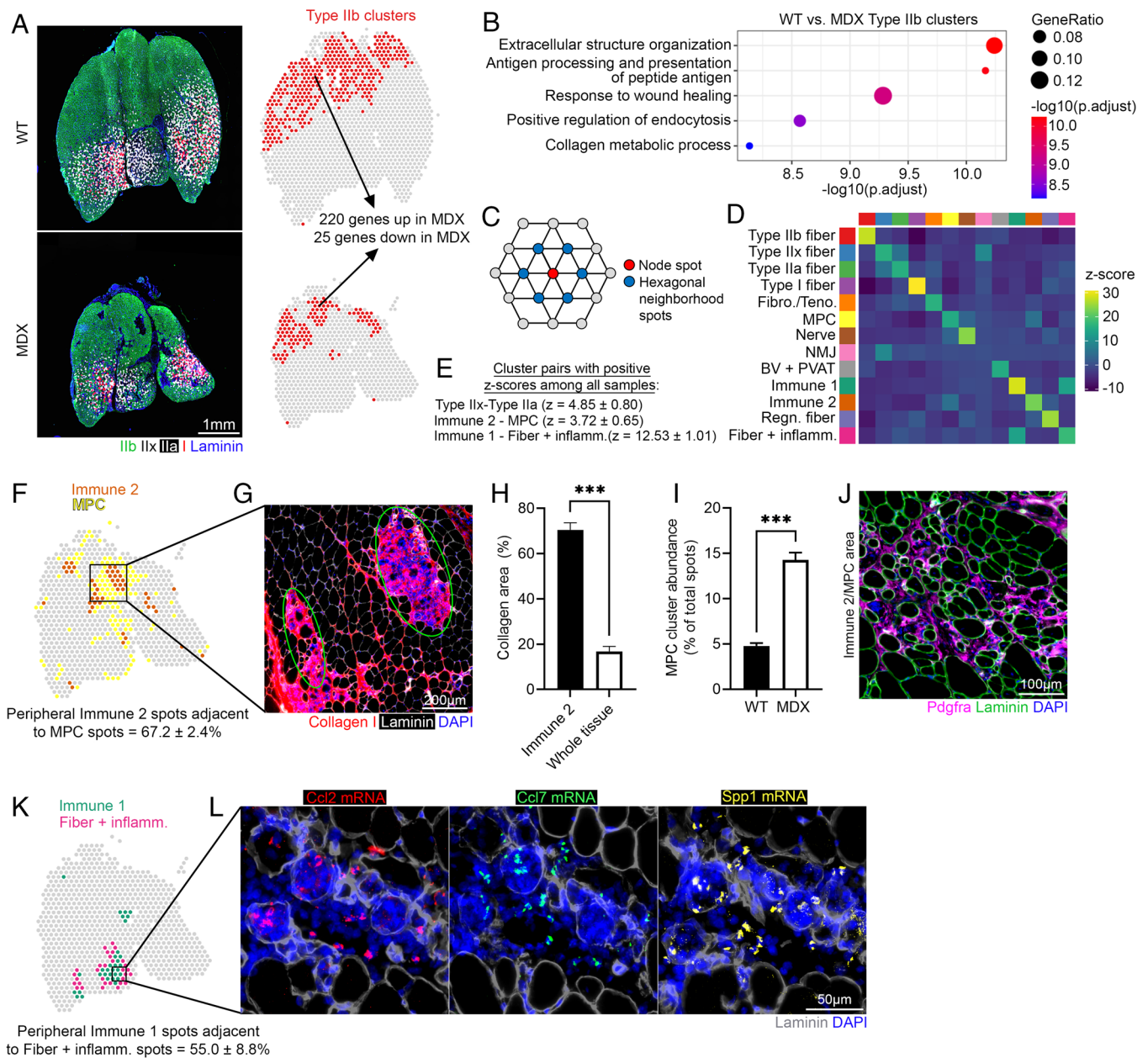
Fig. 5. Fibrosis and inflammation within dystrophic muscle is propagated from areas of localized damage. (*A*) Fiber-type immunostaining and Type IIb fiber cluster localization depicting undamaged Type IIb fiber areas in WT and MDX tissue that were selected for differential gene expression analysis. (*B*) Top five Gene Ontology (biological process) pathways up-regulated in MDX Type IIb fiber clusters compared to WT. Gene ratio is the total number of DEGs divided by the total number of genes each geneset, and the adjusted *P* value is based on gene set enrichment analysis. (*C*) Schematic depicting classification of spatial transcriptomics node spots and neighborhood set spots for Squidpy nearest neighbor analysis. (*D*) Representative neighborhood enrichment analysis between clusters within the MDX3 sample. (*E*) Cluster pairs with positive z-score neighborhood enrichment among all samples containing indicated clusters (n = 4 to 5) (*F*) Localization of Immune 2 and MPC clusters and quantification of the proportion of peripheral Immune 2 spots directly adjacent to MPC spots among all 5 MDX samples (mean ± SEM). (*G*) Immunostaining for collagen I in serial sections corresponding to Immune 2 and MPC cluster areas. Circled areas align with Immune 2 clusters. (*H*) Quantification of collagen I immunostaining in Immune 2 areas compared with the remainder of the tissue section (n = 5; bars indicate mean ± SEM; ***P < 0.001, unpaired t test). (*I*) Quantification of the number of MPC cluster spots in WT and MDX muscle (n = 5; bars indicate mean ± SEM; ***P < 0.001, unpaired t test). (*J*) Immunostaining for localization of Pdgfra+ cells within Immune 2/MPC areas. (*K*) Localization of Immune 1 and Fiber + inflamm. clusters and quantification of the proportion of peripheral Immune 1 spots directly adjacent to Fiber + inflamm. spots among MDX samples (n = 4; mean ± SEM). (*L*) RNAscope imaging for *Ccl2, Ccl7*, and *Spp1* mRNA within Immune 1/Fiber + inflamm. areas.

validated in these areas by RNAscope ISH staining of serial sections (Fig. 5*L*). Additionally, to gain a better understanding of which cells may be producing these signals within Immune 1 cluster areas, we analyzed their expression pattern in single-cell populations and found that granulocyte and macrophage populations that were abundant during an early timepoint following injury had the highest levels of expression of *Ccl2, Ccl7*, and *Spp1* (*SI Appendix,* Fig. S9). When overexpressed in healthy muscle,

the chemokines Ccl2 and Ccl7 induce massive macrophage infiltration and muscle damage (30). Alternatively, when the receptor for these chemokines (*Ccr2*) is ablated in mdx mice, proinflammatory macrophage accumulation is reduced, and muscle pathology is improved (31). Osteopontin (encoded by the Spp1 gene) is a secreted protein that is highly expressed in dystrophic muscle, and genetic ablation of Spp1 in mdx mice reduces inflammatory cell infiltration and fibrosis and improves muscle pathology (32,

33). Given that *Ccl2*, *Ccl7*, and *Spp1* are the most highly expressed genes in the earliest phase of dystrophic muscle regeneration (i.e., Immune 1 areas), secretion of these factors likely plays a major role in promoting the cascade of proinflammatory and profibrotic signaling within and around newly damaged areas. Altogether, these spatial analyses support that the propagation of cellular and molecular signals from areas of localized damage contributes to widespread inflammation and fibrosis in dystrophic muscle.

Discussion

It has long been acknowledged that muscle damage and repair throughout DMD muscle is nonuniform and that asynchronous muscle damage/repair may be a major mechanism driving failed regeneration and muscle pathology (10). Using spatial transcriptomics profiling, we found that the severely dystrophic D2-mdx mouse model faithfully recapitulates the asynchronous degeneration pathology seen in human DMD biopsies (8, 10). Unbiased spatial profiling identified multiple cell clusters with nonuniform distribution throughout D2-mdx muscle and with unique gene expression signatures that predicted the regenerative state of their respective tissue areas. Follow-up immunostaining with validated markers of muscle degeneration/regeneration, along with spatial mapping of MDX cell clusters to acutely damaged WT muscle, confirmed the distinct regenerative state of each cluster. To provide further resolution to our spatial analysis, we performed deconvolution using a skeletal muscle single-cell RNAseq dataset and found that the areas of early regeneration (Immune 1 clusters) were enriched for GN and proliferating muscle stem cells, the areas representing an intermediate stage of regeneration (Immune 2 clusters) were enriched for multiple macrophage populations, and the areas of late-stage regeneration (Regn. fiber clusters) were enriched for fusing myoblasts and pericytes. Thus, in a dystrophic animal model, we have defined a cellular and molecular signature of asynchronous degeneration that maintains spatial resolution.

A unique aspect of our spatial atlas is that it can be used to gain a better understanding of how asynchronous muscle regeneration may contribute to DMD pathology. Previously, Dadgar et al. (10) showed via laser capture microdissection that adjacent focal injuries in wild-type mouse muscle separated by a short interval (4 d) between injuries result in heightened inflammatory signaling in the undamaged area between the two injuries. In contrast, focal injuries separated by a longer interval (10 d) resulted in heightened fibrotic signaling and collagen deposition in undamaged areas between injuries. Surprisingly, when we spatially profiled undamaged tissue regions surrounding damaged/regenerating dystrophic tissue areas, we had strikingly similar observations, with these undamaged areas displaying heightened inflammatory and fibrotic gene expression profiles. In concordance with Dadgar et al.'s data (10), we found that areas surrounding early damaged areas (Fiber + inflamm. clusters) had high inflammatory gene expression, whereas areas surrounding damaged areas in an intermediate state of regeneration were enriched for FAPs and had increased collagen deposition. These data support that within dystrophic tissue, recently damaged areas can emanate inflammatory signals to surrounding healthy muscle, and regenerating areas can propagate the spread of fibrogenic cells to surrounding healthy muscle, thereby driving widespread inflammation and fibrosis throughout the entire tissue. Given that asynchronous degeneration/regeneration, whether driven by focal injuries to WT muscle or by muscular dystrophy, appears to drive global tissue pathology, it is likely that the cellular and molecular findings reported here may be relevant to many chronic inflammatory conditions in which asynchronous damage occurs. Thus, it supports the concept that re-synchronization of tissue regeneration via anti-inflammatory treatment is a mechanism for improving the dystrophic phenotype and that novel therapies targeting pathways involved in asynchronous regeneration could benefit patients with chronic inflammatory conditions beyond DMD.

Our spatial dataset can be easily queried to further examine how localized signaling and cell–cell communication regulates dystrophic disease progression. For example, cell-specific genes or downstream signaling target genes can be spatially mapped to explore the presence of specific cell types or activated signaling pathways within damaged or regenerating areas. Additionally, predicted cell-type co-occurrence within defined tissue areas and neighborhood enrichment analysis can provide information on how cell–cell cross talk may mediate disease processes. While probing our spatial atlas can be useful for understanding DMD disease biology, these types of analyses can also be applied as a tool for drug discovery. For example, we found that the top up-regulated genes in Immune 1 areas are the secreted factors Ccl2, Ccl7, and Spp1, which are known regulators of DMD disease progression in mouse models (30–33). Additionally, Spp1 genotype has been shown to be a genetic modifier of human DMD disease severity (34, 35), further supporting therapeutic targeting of this factor in damaged areas of DMD tissue. By showing that these chemokine/profibrotic factors are increased in regions of early muscle damage (containing primarily GN and proinflammatory macrophages), before significant fibrosis occurs, it provides rationale for therapeutically targeting these factors to prevent downstream muscle inflammation and fibrosis.

While our spatial atlas of dystrophic muscle provides a much-needed resource for the study of DMD biology and therapeutic target discovery, it does have limitations. For example, the 55-μm-diameter probe spots used here do not provide enough resolution for small, sparsely distributed populations to be detected as unique clusters—such as low abundance MuSC and macrophage populations scattered throughout WT muscle that were not detected as clusters. However, this limitation was partially addressed by performing cellular deconvolution, which McKellar et al. (17) have shown greatly enhances spatial transcriptomics resolution and detection of multiple cell subtypes within injured skeletal muscle. Our cellular deconvolution of MDX muscle aided in defining localization of many small cell populations, although with the caveat that it was performed using a skeletal muscle single-cell RNAseq dataset that was taken from injured wild-type mouse muscle (20). Given that there are likely differences in gene expression profiles between some populations of wild-type and dystrophic cells, future cellular deconvolution of this dataset could be performed with single cells isolated from D2-mdx mice; although the use of an injured wild-type mouse muscle dataset provides us more clarity in defining cell populations over a defined regenerative timecourse. Finally, another potential limitation of this study is that the experiments were performed in dystrophic and damaged mouse skeletal muscle as opposed to human tissue. However, the D2-mdx mouse is one of the most relevant models of DMD, displaying clear asynchronous degeneration/regeneration and similar histopathology to human DMD muscle, likely due to mutation in the Ltbp4 gene in this strain (36, 37), which is a known disease modifying gene in human DMD (38, 39). Future spatial profiling studies should be performed on human DMD biopsies to validate our findings in the context of human disease.

In summary, the spatial atlas of dystrophic muscle described here is an invaluable resource for the study of DMD disease biology and therapeutic target discovery. The asynchronous degeneration observed here in D2-mdx muscle serves as a clinically relevant model of human DMD, and thus, this cellular and molecular profiling database may offer important translational insight.

Additionally, by maintaining spatial context and clearly defining local tissue microenvironments, this dataset provides a significant advancement over current dystrophic muscle -omics dataset.

Materials and Methods

Tissue Processing for Spatial Transcriptomics. All animal procedures were performed in accordance with the Regeneron Institutional Animal Care and Use Committee (IACUC). Six-wk-old male wild-type (DBA2/J from Jackson Laboratory, stock #000671; n = 3) and severely dystrophic (D2-mdx from Jackson Laboratory, stock #013141; n = 5) mice were killed, and the gastrocnemius/plantaris muscle complex was immediately frozen in optimal cutting temperature cryomolds in liquid nitrogen–cooled isopentane and stored at −80 °C. Test muscle samples were cryosectioned at 10 μm thickness onto Visium tissue optimization slides and processed according to manufacturer guidelines, and the optimal enzyme permeabilization time for maximal mRNA release was found to be 12 min. Samples were then sectioned onto Visium spatial gene expression slides, and serial sections within ~50 μm distance from the Visium slide section were collected onto SuperFrost Plus charged slides for follow-up immunostaining and RNA ISH. For immunofluorescence-coupled spatial transcriptomics experiments to examine CD31+ blood vessel/capillary localization and gene expression throughout the regenerative timecourse, adult C57BL/6 muscle was processed via methanol fixation and immunofluoresence staining according to the manufacturer's guidelines using the antibodies described below. For injury experiments, adult mice were anesthetized with isoflurane, their leg was shaved, and the left lateral gastrocnemius was intramuscularly injected with 50 μL of 10 μM cardiotoxin (diluted in 0.9% saline; Sigma, 217503). Tissue was collected at 1, 3, and 5 d post injury for spatial transcriptomics profiling.

Visium Gene Expression Slide Processing and Library Sequencing. Tissue sections were fixed in prechilled methanol for 30 min, and H&E staining was performed per the published protocol from 10× Genomics. Imaging was done using a Zeiss Axio Observer microscope, and images were stitched and processed using Zen 2.0 software. Following tissue permeabilization, spatially tagged cDNA libraries were built using the 10× Genomics Visium Spatial Gene Expression Library Construction Kit. Sequencing was performed on an Illumina NextSeq 500/550 using 150-cycle High Output kits (read 1 = 28, read 2 = 120, index 1 = 10, and index 2 = 10). Mouse genome reference mm10 (Ensembl93) and gene annotation (GRCm38) were downloaded from ENSEMBL and Reference Sequence, and Spaceranger 1.0.0 (10× Genomics) was used to process, align, and summarize UMI counts against mm10 mouse reference genome for each spot on each sample. Alignment of H&E images was done using Loupe Browser.

Spatial Transcriptomics Spot Deconvolution. For cell-type deconvolution, we used single-cell populations obtained from the atlas of muscle regeneration in adult mice (20) (GEO:GSE143437) to predict spot content for all samples. To separate cell clusters, we downloaded the raw UMI data from GEO and performed log normalization, principal component analysis (PCA), nearest-neighbor graph construction, and cluster determination from Seurat V3 package with default parameters setting. Cell-type deconvolution was calculated for each spot using a stereoscope (21) with default parameters. Cell-type colocalization values used in the chord diagram were calculated by counting cell-type pair abundances in spatial spots. Only cell types with prediction scores larger than 10% in a given spot were included.

Immunofluorescence. Serial sections adjacent to the spatially profiled section were fixed with 4% paraformaldehyde (PFA) for 15 min and washed three times with phosphate buffered saline (PBS). Sections were incubated in blocking solution [20% goat serum (or 4% bovine serum albumin, BSA, when staining for PDGFRα), 0.3% Triton X-100 in 1× PBS] for 1 h and then incubated in primary antibodies overnight (1:100, unless otherwise stated, in blocking solution). After three PBS washes, slides were incubated for 1 h in filtered secondary antibody solution (1:250 in blocking solution). Slides were counterstained with Hoechst 33342 (1:1000; ThermoFisher, H3570) for 5 min, washed with PBS, and then mounted in Fluoromount G (ThermoFisher, 00-4958-02). For fiber-type staining, sections were permeabilized with 0.1% Triton X-100 for 10 min and then incubated in 4% BSA for 1 h. Then, sections were incubated with primary antibodies (1:100) for 1 h and after three PBS washes were incubated in filtered secondary antibody

solution for 1 h. After three more PBS washes, sections were fixed with 4% PFA for 15 min and then counterstained and mounted as earlier described. Sections were imaged using a Zeiss Axioscan microscope and processed using HALO software (Indica Labs). Primary antibodies were as follows: laminin (Sigma-Aldrich, L9393 & 1:500; Abcam, ab11576), F-actin (1:500; Invitrogen, A22287), collagen I (Abcam, ab270993), F4/80 (Abcam, ab6640), perilipin (Cell Signaling, 9349S), CD31 (BioLegend, 102504), CD68 (Abcam, ab201845), CD206 (Cell Signaling, 24595S), wheat germ agglutinin (1:500; Invitrogen, W32466), mIgG (Invitrogen, A32723), PDGFRa (R&D Systems, AF1062), MHC isoforms [MHC type I, BA-D5; MHC type IIA, SC-71; MHC type IIb, BF-F3; Developmental Studies Hybridoma Bank (DSHB), University of Iowa], neurofilament (1:50; DSHB, 2H3), and α-bungarotoxin (1.5 μg/mL; ThermoFisher, B13426). The primary antibodies were detected with the appropriate Alexa fluorophore 488, 546, or 647 secondary antibodies (ThermoFisher).

ISH. Serial sections were prepared for RNAscope® assay according to the Advanced Cell Diagnostics (ACD) protocol for fresh frozen tissue (Document number 320513, ACD). RNAscope® was performed according to the manufacturer's protocol RNAscope® Multiplex Fluorescent Assay V2 (Document Number 320293-USM, ACD). Prior to counterstaining, the section was incubated in laminin primary antibody solution with (1:100 in blocking solution; Sigma, L9393) for 30 min. Slides were washed with PBS two times and then incubated for 30 min in filtered secondary antibody solution (1:250 in blocking solution). Slides were then washed with PBS, counterstained according to the manufacturer's protocol, and then mounted using Fluoromount-G. Sections were imaged using a Zeiss Axioscan microscope and processed using HALO software. RNAscope® probes used were as follows: Mm-Spp1-C2 (ACD, 435191-C2), Mm-Ccl7 (ACD, 446821), Mm-Ccl2-C3 (ACD, 311791-C3), and probe diluent (ACD 300041) when appropriate. The primary antibody was detected with Alexa fluorophore 488 (ThermoFisher, 32731).

Statistical Analysis. Data are expressed as mean ± SEM. Statistical analyses were performed using GraphPad Prism version 9. Unpaired two-tailed Student t tests were performed for statistical comparision between groups, with $P < 0.05$ being considered statistically significant.

For spatial transcriptomics data analysis processing, raw UMI counts from spots covered by tissue were normalized using regularized negative binomial regression (SC Transform) (40) from the Seurat V3 package to account for variability of RNA content within each spot. PCA was performed for each phenotype group, and the optimum number of principal components was determined by examining the scree plots. Uniform Manifold Approximation and Projection (UMAP) was initialized in this PCA space to visualize the data on reduced UMAP dimensions. The spots were clustered (WT and MDX samples clustered separately) on PCA space using the Louvain clustering algorithm implemented as FindNeighbors and FindClusters in Seurat with parameters k = 20 and resolution = 0.8 and 0.6 (for WT and MDX, respectively). Spot cluster representation was then visualized on UMAP space and spatial context over H&E images using the SpatialPlot command.

For labeling anatomical regions, the Wilcox test was performed to find differentially expressed genes for each region/cluster. The FindMarkers function in Seurat with its default parameters was used to get a list of differentially expressed genes for each cluster (FDR < 0.01, fold change ≥ 1.5). Gene expression was visualized using the SpatialPlot function from Seurat.

To identify differentially expressed genes between WT and MDX clusters, we combined both WT and MDX spots and normalized using SCTransform. Then, the FindMarkers function was used with its default parameter. For each comparison (cluster level), we compared the spots from WT versus MDX within a given cluster. For GO enrichment analysis, we selected significant genes with FDR < 0.01 and fold change ≥ 1.5 and used the default enrichGO implemented in clusterProfile R package for enrichment analysis of GO terms representing various Biological Processes (BP).

To compute the neighborhood enrichment between each MDX cluster, nhood_enrichment function in Squidpy was used with its default parameter (25). To follow-up on enriched cluster pairs, the proportion of peripheral Immune 1 or Immune 2 spots was manually counted, and the percentage of those spots that were directly adjacent to Fiber + inflamm. or MPC spots, respectively, was quantified.

To compute the module score of 1 dpi, 3 dpi, and 5 dpi cardiotoxin-injured muscle, we selected 10 top cluster enriched genes based on the adjusted

P value from MDX Immune 1, Immune 2, and Regn. fiber clusters and used the AddModuleScore function in Seurat with its default parameter.

Author affiliations: [a]Regeneron Pharmaceuticals, Tarrytown, NY 10591; [b]Department of Physiology and Biophysics, University of California Irvine, Irvine, CA 92697; [c]Institute for Immunology, University of California Irvine, Irvine, CA 92697; and [d]Department of Neurology, University of California Irvine, Irvine, CA 92697

1. A. S. Kesselheim, J. Avorn, Approving a problematic muscular dystrophy drug: Implications for FDA policy. *JAMA* **316**, 2357–2358 (2016).
2. Y. Shimizu-Motohashi, T. Murakami, E. Kimura, H. Komaki, N. Watanabe, Exon skipping for duchenne muscular dystrophy: A systematic review and meta-analysis. *Orphanet J. Rare Dis.* **13**, 93 (2018).
3. D. Duan, Systemic AAV micro-dystrophin gene therapy for duchenne muscular dystrophy. *Mol. Ther.* **26**, 2337–2356 (2018).
4. L. Morales, Y. Gambhir, J. Bennett, H. H. Stedman, Broader implications of progressive liver dysfunction and lethal sepsis in two boys following systemic high-dose AAV. *Mol. Ther.* **28**, 1753–1755 (2020).
5. C. M. McDonald et al., Long-term effects of glucocorticoids on function, quality of life, and survival in patients with duchenne muscular dystrophy: a prospective cohort study. *Lancet* **391**, 451–461 (2018).
6. L. Cowen, M. Mancini, A. Martin, A. Lucas, J. M. Donovan, Variability and trends in corticosteroid use by male United States participants with duchenne muscular dystrophy in the duchenne registry. *BMC Neurol.* **19**, 84 (2019).
7. M. Guglieri et al., Efficacy and safety of vamorolone vs. placebo and prednisone among boys with duchenne muscular dystrophy: a randomized clinical trial. *JAMA Neurol.* **79**, 1005–1014 (2022).
8. A. S. Rosenberg et al., Immune-mediated pathology in duchenne muscular dystrophy. *Sci. Transl. Med.* **7**, 299rv294 (2015).
9. M. N. Wosczyna, T. A. Rando, A muscle stem cell support group: coordinated cellular responses in muscle regeneration. *Dev. Cell* **46**, 135–143 (2018).
10. S. Dadgar et al., Asynchronous remodeling is a driver of failed regeneration in duchenne muscular dystrophy. *J. Cell Biol.* **207**, 139–158 (2014).
11. F. Chemello et al., Degenerative and regenerative pathways underlying duchenne muscular dystrophy revealed by single-nucleus RNA sequencing. *Proc. Natl. Acad. Sci. U.S.A.* **117**, 29691–29701 (2020).
12. M. Kim et al., Single-nucleus transcriptomics reveals functional compartmentalization in syncytial skeletal muscle cells. *Nat. Commun.* **11**, 6375 (2020).
13. P. Podkalicka et al., Lack of miR-378 attenuates muscular dystrophy in mdx mice. *JCI Insight* **5**, e135576 (2020).
14. T. C. Roberts et al., Expression analysis in multiple muscle groups and serum reveals complexity in the MicroRNA transcriptome of the mdx mouse with implications for therapy. *Mol. Therapy - Nucleic Acids* **1**, e39 (2012).
15. T. C. Roberts, K. E. M. Blomberg, C. I. E. Smith, S. El Andaloussi, M. J. A. Wood, mRNA and microRNA transcriptomics analyses in a murine model of dystrophin loss and therapeutic restoration. *Genom. Data* **7**, 88–89 (2016).
16. B. Malecova et al., Dynamics of cellular states of fibro-adipogenic progenitors during myogenesis and muscular dystrophy. *Nat. Commun.* **9**, 3670 (2018).
17. D. W. McKellar et al., Large-scale integration of single-cell transcriptomic data captures transitional progenitor states in mouse skeletal muscle regeneration. *Commun. Biol.* **4**, 1280 (2021).
18. C. D'Ercole et al., Spatially resolved transcriptomics reveals innervation-responsive functional clusters in skeletal muscle. *Cell Rep.* **41**, 111861 (2022).
19. G. Panci, B. Chazaud, Inflammation during post-injury skeletal muscle regeneration. *Semin. Cell Dev. Biol.* **119**, 32–38 (2021).
20. A. J. De Micheli et al., Single-cell analysis of the muscle stem cell hierarchy identifies heterotypic communication signals involved in skeletal muscle regeneration. *Cell Rep.* **30**, 3583–3595.e3585 (2020).
21. A. Andersson et al., Single-cell and spatial transcriptomics enables probabilistic inference of cell type topography. *Commun. Biol.* **3**, 565 (2020).
22. J. Dort, P. Fabre, T. Molina, N. A. Dumont, Macrophages are key regulators of stem cells during skeletal muscle regeneration and diseases. *Stem Cells Int.* **2019**, 4761427–4761427 (2019).
23. M. Saclier et al., Differentially activated macrophages orchestrate myogenic precursor cell fate during human skeletal muscle regeneration. *Stem Cells* **31**, 384–396 (2013).
24. J. G. Tidball, S. A. Villalta, Regulatory interactions between muscle and the immune system during muscle regeneration. *Am. J. Physiol. Regul. Integr. Comp. Physiol.* **298**, R1173–R1187 (2010).
25. G. Palla et al., Squidpy: A scalable framework for spatial omics analysis. *Nat. Methods* **19**, 171–178 (2022).
26. C. Moratal, N. Arrighi, C. A. Dechesne, C. Dani, Control of muscle fibro-adipogenic progenitors by myogenic lineage is altered in aging and duchenne muscular dystrophy. *Cell Physiol. Biochem.* **53**, 1029–1045 (2019).
27. C. Mozzetta et al., Fibroadipogenic progenitors mediate the ability of HDAC inhibitors to promote regeneration in dystrophic muscles of young, but not old Mdx mice. *EMBO Mol. Med.* **5**, 626–639 (2013).
28. A. W. B. Joe et al., Muscle injury activates resident fibro/adipogenic progenitors that facilitate myogenesis. *Nat. Cell Biol.* **12**, 153–163 (2010).
29. S. N. Oprescu, F. Yue, J. Qiu, L. F. Brito, S. Kuang, Temporal dynamics and heterogeneity of cell populations during skeletal muscle regeneration. *iScience* **23**, 100993 (2020).
30. H. Zhu et al., STAT3 regulates self-renewal of adult muscle satellite cells during injury-induced muscle regeneration. *Cell Rep.* **16**, 2102–2115 (2016).
31. K. Mojumdar et al., Inflammatory monocytes promote progression of duchenne muscular dystrophy and can be therapeutically targeted via CCR2. *EMBO Mol. Med.* **6**, 1476–1492 (2014).
32. J. Capote et al., Osteopontin ablation ameliorates muscular dystrophy by shifting macrophages to a pro-regenerative phenotype. *J. Cell Biol.* **213**, 275–288 (2016).
33. S. A. Vetrone et al., Osteopontin promotes fibrosis in dystrophic mouse muscle by modulating immune cell subsets and intramuscular TGF-beta. *J. Clin. Invest.* **119**, 1583–1594 (2009).
34. M. Chen et al., Genetic modifiers of duchenne muscular dystrophy in chinese patients. *Front. Neurol.* **11**, 721 (2020).
35. E. Pegoraro et al., SPP1 genotype is a determinant of disease severity in duchenne muscular dystrophy. *Neurology* **76**, 219–226 (2011).
36. A. Heydemann et al., Latent TGF-β–binding protein 4 modifies muscular dystrophy in mice. *J. Clin. Invest.* **119**, 3703–3712 (2009).
37. D. W. Hammers et al., The D2.mdx mouse as a preclinical model of the skeletal muscle pathology associated with duchenne muscular dystrophy. *Sci. Rep.* **10**, 14070 (2020).
38. K. M. Flanigan et al., LTBP4 genotype predicts age of ambulatory loss in duchenne muscular dystrophy. *Ann. Neurol.* **73**, 481–488 (2013).
39. J. C. v. d. Bergen et al., Validation of genetic modifiers for Duchenne muscular dystrophy: A multicentre study assessing SPP1 and LTBP4 variants. *J. Neurol. Neurosurg. Psychiatry* **86**, 1060–1065 (2015).
40. C. Hafemeister, R. Satija, Normalization and variance stabilization of single-cell RNA-seq data using regularized negative binomial regression. *Genome Biol.* **20**, 296 (2019).
41. Q. Su et al., Spatial Transcriptiomics of Mouse Skeletal Muscle. NCBI Gene Expression Omnibus. https://www.ncbi.nlm.nih.gov/geo/query/acc.cgi?acc=GSE225766. Deposited 21 February 2023.